A systematic fitting scheme for caustic-crossing microlensing events

N. Kains,[1,2]★ A. Cassan,[1,3] K. Horne,[1,2] M. D. Albrow,[1,4] S. Dieters,[1,5] P. Fouqué,[1,6]
J. Greenhill,[1,7] A. Udalski,[8,9] M. Zub,[1,3]† D. P. Bennett,[1,10] M. Dominik,[2]‡
J. Donatowicz,[1,11] D. Kubas,[1,12] Y. Tsapras,[1,13] T. Anguita,[3] V. Batista,[1,5]
J.-P. Beaulieu,[1,5] S. Brillant,[1,12] M. Bode,[1,13] D. M. Bramich,[1,14] M. Burgdorf,[1,13]
J. A. R. Caldwell,[1,15] K. H. Cook,[1,16] Ch. Coutures,[1,17] D. Dominis Prester,[1,18]
U. G. Jørgensen,[1,19] S. Kane,[1,20] J. B. Marquette,[1,5] R. Martin,[1,21] J. Menzies,[1,22]
K. R. Pollard,[1,4] N. Rattenbury,[1,23] K. C. Sahu,[1,24] C. Snodgrass,[1,12] I. Steele,[1,11]
C. Vinter,[1,19] J. Wambsganss,[1,3] A. Williams,[1,21] M. Kubiak,[8,9] G. Pietrzyński,[8,9,25]
I. Soszyński,[8,9] O. Szewczyk,[8,9,25] M. K. Szymański,[8,9] K. Ulaczyk[8,9]
and Ł. Wyrzykowski[13,26]

[1] *PLANET/RoboNet Collaborations*
[2] *SUPA, School of Physics and Astronomy, University of St. Andrews, North Haugh, St Andrews KY16 9SS*
[3] *Astronomisches Rechen-Institut (ARI), Zentrum für Astronomie (ZAH), Heidelberg University, Mönchhofstraße 12-14, 69120 Heidelberg, Germany*
[4] *Department of Physics and Astronomy, University of Canterbury, Private Bag 4800, Christchurch, New Zealand*
[5] *Institut d'Astrophysique de Paris, UMR7095 CNRS, Université Pierre & Marie Curie, 98bis Boulevard Arago, 75014 Paris, France*
[6] *LATT, Université de Toulouse, CNRS, 14 avenue Edouard Belin, F-31400 Toulouse, France*
[7] *School of Mathematics and Physics, University of Tasmania, Private Bag 37, Hobart, Tasmania 7001, Australia*
[8] *Optical Gravitational Lens Experiment (OGLE) Collaboration*
[9] *Warsaw University Observatory, Al. Ujazdowskie 4, 00-478 Warszawa, Poland*
[10] *Department of Physics, University of Notre Dame, 225 Nieuwland Science Hall, Notre Dame, IN 46556, USA*
[11] *Department of Computing, Technical University of Vienna, Wiedner Hauptstr. 10, Vienna A-1040, Austria*
[12] *European Southern Observatory, Casilla 19001, Vitacura 19, Santiago, Chile*
[13] *Astrophysics Research Institute, Liverpool John Moores University, Twelve Quays House, Egerton Wharf, Birkenhead CH41 1LD*
[14] *Isaac Newton Group of Telescopes, Apartado de Correos 321, E-38700 Santa Cruz de La Palma, Spain*
[15] *McDonald Observatory, 16120 St Hwy Spur 78, Fort Davis, TX 79734, USA*
[16] *Lawrence Livermore National Laboratory, IGPP, PO Box 808, Livermore, CA 94551, USA*
[17] *DSM/DAPNIA, CEA Saclay, 91191 Gif-sur-Yvette cedex, France*
[18] *Physics Department, Faculty of Arts and Sciences, University of Rijeka, 51000 Rijeka, Croatia*
[19] *Niels Bohr Institute, Astronomical Observatory, Juliane Maries Vej 30, DK-2100 Copenhagen, Denmark*
[20] *NASA Exoplanet Science Institute, Caltech, MS 100-22, 770 South Wilson Avenue, Pasadena, CA 91125, USA*
[21] *Perth Observatory, Walnut Road, Bickley, Perth 6076, Australia*
[22] *South African Astronomical Observatory, PO Box 9, Observatory 7935, South Africa*
[23] *Jodrell Bank Centre for Astrophysics, University of Manchester, Manchester M13 9PL*
[24] *Space Telescope Science Institute, 3700 San Martin Drive, Baltimore, MD 21218, USA*
[25] *Departamento de Fisica, Astronomy Group, Universidad de Concepción, Casilla 160-C, Concepción, Chile*
[26] *Institute of Astronomy, University of Cambridge, Madingley Road, Cambridge CB3 0HA*

ABSTRACT

We outline a method for fitting binary-lens caustic-crossing microlensing events based on the alternative model parametrization proposed and detailed by Cassan. As an illustration of our methodology, we present an analysis of OGLE-2007-BLG-472, a double-peaked Galactic microlensing event with a source crossing the whole caustic structure in less than three days.

★ E-mail: nk87@st-and.ac.uk
† Member of International Max Planck Research School for Astronomy and Cosmic Physics at the University of Heidelberg.
‡ Royal Society University Research Fellow.

In order to identify all possible models we conduct an extensive search of the parameter space, followed by a refinement of the parameters with a Markov Chain Monte Carlo algorithm. We find a number of low-χ^2 regions in the parameter space, which lead to several distinct competitive best models. We examine the parameters for each of them, and estimate their physical properties. We find that our fitting strategy locates several minima that are difficult to find with other modelling strategies and is therefore a more appropriate method to fit this type of event.

Key words: gravitational lensing – methods: miscellaneous – binaries: general – planetary systems – Galaxy: bulge.

1 INTRODUCTION

Gravitational microlensing (Paczyński 1986) occurs when the light from a source star is deflected by a massive compact object between the source and the observer, leading to an apparent brightening of the source, typically lasting a few days to a few weeks. When the deflecting body has multiple components, such as a planet orbiting its host star, there can be perturbations to the brightening pattern of observed sources. These perturbations can be large even when caused by low-mass objects, making them detectable using small ground-based telescopes. Modelling these light-curve anomalies can lead to the detection of subtle effects, allowing for measurements of properties such as the source star limb-darkening coefficients (e.g. Cassan et al. 2004), the mass of stars with no visible companions (e.g. Ghosh et al. 2004) and the detection of extrasolar planets, as suggested by Mao & Paczyński (1991) and first achieved in 2003 (Bond et al. 2004).

Nevertheless, anomalous microlensing events usually require very detailed analysis for a full characterization of their nature to be possible. This applies in particular to a class of microlensing events which display caustic-crossing features in their light curves. These events are of primary interest, because they account for around 10 per cent of the overall number of detected microlenses, and they represent an important source of information on physical properties of binary stars (Jaroszynski et al. 2006). However, there exist several degeneracies that affect the modelling of this type of event. Without a robust modelling scheme and a full exploration of the parameter space, it is impossible to pin down the true nature of a given event. In addition to this, calculations of anomalous microlensing models for extended sources are very demanding computationally.

Given these issues, brute force is not an option when modelling caustic-crossing events, and one has to devise ways of speeding up calculations, for example by excluding regions of parameter space which cannot reproduce features that appear in data sets. A way to achieve this is to use a non-standard parametrization of the binary-lens models that ties them directly to data features, as proposed by Cassan (2008), which we recall below.

In this paper, we present our method for exploring the parameter space, and describe our approach to find all possible models for a given event (Section 2). We then use OGLE-2007-BLG-472, a microlensing event observed in 2007 by the Optical Gravitational Lens Experiment (OGLE) and Probing Lensing Anomalies NETwork (PLANET) collaborations, as an illustration of our methodology applied to a binary-lens event which intrinsically harbours many ambiguities (Section 3). We finally discuss the implications of the individual competitive models that we find in order to discriminate between realistic microlensing scenarios.

2 BINARY-LENS EVENTS FITTING SCHEME

2.1 Parametrization of binary-lens light curves

A static binary lens is usually described by the mass ratio $q < 1$ of the two lens components and by their separation d, expressed in units of the angular Einstein radius (Einstein 1936):

$$\theta_E = \sqrt{\frac{4GM}{c^2}\left(\frac{D_S - D_L}{D_S D_L}\right)}, \tag{1}$$

where M is the mass of the lens, and D_L and D_S are the distances to the lens and the source, respectively. Such a lens produces caustics where the magnification of the source diverges to infinity for a perfect point source. The positions, sizes and shapes of the caustics depend on d and q. For the binary-lens case, caustics can exist in three different topologies, usually referred as *close*, *intermediate* and *wide*; bifurcation values between these topologies are analytical expressions relating d with q (Erdl & Schneider 1993). In the close regime, there are three caustics: a *central* caustic near the primary lens component, and two *secondary* caustics which lie off the axis passing through both lens components. In the intermediate case, there is only one large caustic on the axis. In the wide case, there is a *central* as well as a *secondary* caustic, both on the axis. The limits between these configurations are indicated as the dashed lines in e.g. Fig. 2 (see also fig. 1 of Cassan 2008).

The description of the light curve itself requires four more geometrical parameters in addition to d and q. In the current standard parametrization of binary-lens light curves, these are the source trajectory's angle α with the axis of symmetry of the lens, the time of closest source–lens approach to the binary-lens centre-of-mass t_0, the Einstein radius crossing time t_E and the source–lens separation at closest approach u_0 (in units of θ_E). Finally, for a uniformly bright finite size source star, we add a further parameter, the source size ρ_* in units of θ_E. However, and as discussed in Cassan (2008), this parametrization is not well adapted to conducting a full search of the parameter space, because the value of the parameters cannot be directly related to features present in the light curve, namely caustic crossings for the type of event we are discussing in this paper. Consequently, most of the probed models in a given fitting process do not exhibit the most obvious features in the light curve, leading to very inefficient modelling.

To avoid this drawback, Cassan (2008) introduced a new parametrization in place of α, t_0, u_0 and t_E which is closely related to the appearance of caustic-crossing features in the light curve. The caustic entry is then defined by a date t_{entry} when the source centre crosses the caustic [1] and its corresponding (two-dimensional)

---

[1] Alternatively, any other point at a fixed position from the source centre can be defined as a reference.

coordinate ζ_{entry} on the source plane. However, since by definition this point is located on a caustic line, Cassan (2008) introduced a (one-dimensional) *curvilinear abscissa s* which locates the crossing point directly on the caustic, so that $\zeta_{\text{entry}} \equiv \zeta(s_{\text{entry}})$. A given caustic structure is fully parametrized by $0 \leq s \leq 2$. The caustic entry is then characterized by a pair of parameters $(t_{\text{entry}}, s_{\text{entry}})$, and in the same way the caustic exit by $(t_{\text{exit}}, s_{\text{exit}})$. These four parameters (in addition to d, q and ρ_*) which describe the caustic crossings therefore also define an alternative parametrization of the binary lens, far better suited to describing the problem at hand.

2.2 Exploration of the parameter space

We start by exploring a wide region of the parameter space with a (d, q) grid regularly sampled on a logarithmic scale. This choice comes from the fact that the size of the caustic structures behaves like power laws of the lens separation and mass ratio, as do the corresponding light-curve anomalies. We fit for the remaining model parameters t_{entry}, t_{exit}, s_{entry}, s_{exit} and ρ_*, with (d, q) being held fixed. From this, we then build a $\chi^2(d, q)$ map that we use to locate the best-fitting (d, q) regions. In the wide and close binary cases and following Cassan (2008), we study separately models where the source crosses the central or the secondary caustic by building two $\chi^2(d, q)$ maps, corresponding to each configuration.

In order to sample efficiently and extensively s_{entry} and s_{exit} (which determine the source trajectory), we use a genetic algorithm (e.g. Charbonneau 1995) that always retains the best model from one generation to the next (*elitism*). In fact, since we consider only models displaying caustics at the right positions, there are a couple of local minima associated with different $(s_{\text{entry}}, s_{\text{exit}})$ pairs. These would usually be missed by other minimization methods, but a genetic algorithm naturally solves this problem in an efficient way. However, since such an algorithm never converges exactly to the best model, we finally refine the model by performing a Markov Chain Monte Carlo (MCMC) fit: we start several chains and use the criterion by Geweke (1992) to assess convergence to a stationary posterior distribution of the parameter probability densities.

From the χ^2 maps, we then identify all the local minima regions and use the corresponding best models found on the (d, q) grid as starting points to refine the parameters, including (d, q) that we now allow to vary. Since the fit is performed within a minimum χ^2 region, the fitting process is very stable and fast.

3 APPLICATION TO OGLE-2007-BLG-472

3.1 Alert and photometric follow-up

On 2007 August 19, the OGLE Early Warning System (Udalski 2003) flagged microlensing candidate event OGLE-2007-BLG-472 at right ascension $\alpha_{2000.0} = 17{:}57{:}04.34$, and declination $\delta_{2000.0} = -28{:}22{:}02.1$ or $l = 1°.77$, $b = -1°.87$.

The OGLE light curve has an instrumental baseline magnitude $I = 16.00$, which may differ from the calibrated magnitude by as much as 0.5 mag. Lensing by the star in the point source–point lens (PSPL) approximation accounts for the broad rise and fall in the light curve, peaking around $\text{MHJD}^2 = 4334.0$ with an apparent half-width at half-peak of about 10 d (Fig. 1). Although the observed OGLE flux rises only by 0.06 mag in the non-anomalous part of the light curve, the shape of the curve hints that blending is important
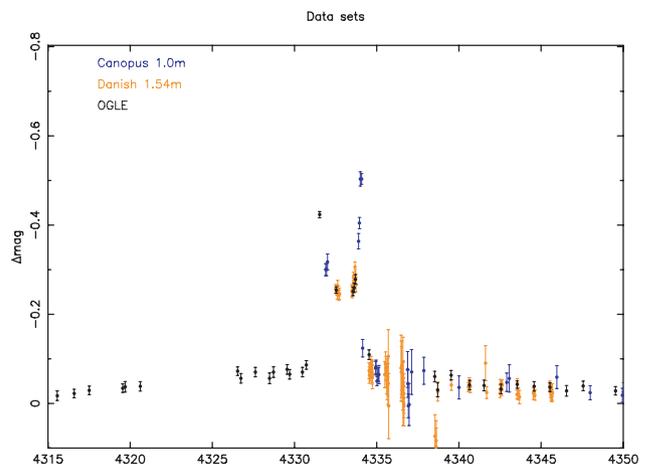
---

² MHJD = HJD 245 0000.

Figure 1. OGLE, UTas and Danish data set for OGLE-2007-BLG-472 data sets. Data points are plotted with 1σ error bars. The *x*-axis is time in HJD−245 0000.

for this target, with only $\sim$12 per cent of the baseline flux due to the unmagnified source.

On August 19 (MHJD = 4331.5) an OGLE data point showed a sudden brightening of the source, with subsequent PLANET (UTas Mt. Canopus 1.0-m telescope in Tasmania and Danish 1.54-m telescope at La Silla, Chile) and OGLE data indicating what appears to be a fold caustic crossing by the source, ending with a PLANET UTas data point on August 21 (MHJD = 4334.1). The caustic entry is observed by a single OGLE point, while the caustic exit is well covered by our UTas data set (Fig. 1). Treating the light curve as the addition of an anomaly to a PSPL light curve, the underlying PSPL curve then apparently reaches peak magnification on August 22 (MHJD = 4335.45). Particularly crucial in our data set is the UTas observation taken within a few hours of the caustic exit, which tightly constrains the position of the caustic exit on the light curve, and on the size of the source. Although *V*-band observations were taken, the *V* light curve of this event does not sample the time when the source was magnified significantly, and therefore does not provide us with constraints on the properties of the source.

3.2 Data reduction

We reduced the PLANET data for this event using the data reduction pipeline PYSIS3.0 (Albrow et al., in preparation). This pipeline uses a kernel as a discrete pixel array, as proposed by Bramich (2008), rather than a linear combination of basis functions. This has the advantage that it removes the need for the user to select basis functions manually, which can lead to problems if inappropriate functions are chosen. In addition to this, the pixel array kernel copes better with images that are not optimally aligned. The result of using this pipeline is a better reduction than was obtained with other methods. We kept all points with seeing <3.5 arcsec. Although some dubious points remain with this simple cut, the size of their associated error bars reflects their lack of certainty and ensures their weight in any modelling procedures is appropriately reduced. Our final data set consists of 34 UTas data points, 84 points from the Danish 1.54-m telescope and 857 points from OGLE (Table 1).
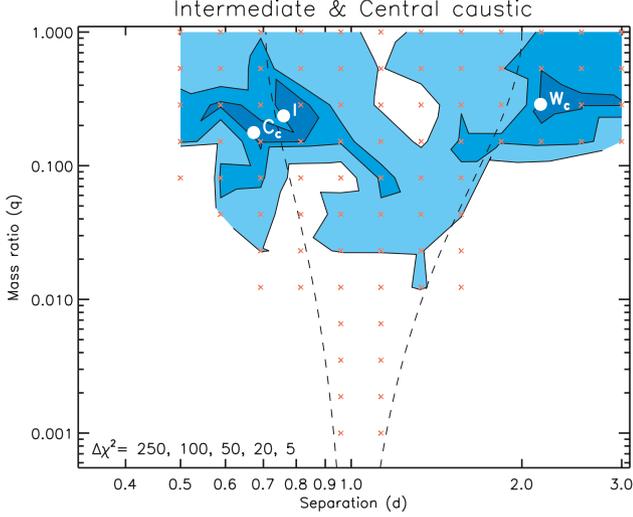
3.3 Modelling OGLE-2007-BLG-472

After a first exploration of the parameter space, we find a best model (close to model C_c, see below) which we use as a basis to rescale our

Table 1. Data sets and error bar rescaling factors.

Telescope	Data	Error bar rescaling factor
UTas 1.0-m	34	1.79
Danish 1.54-m	84	1.55
OGLE	857	1.21

Figure 2. $\chi^2(d, q)$ map for the intermediate and central caustic configurations. Contour lines and minima regions (in blue shades) are plotted at $\Delta\chi^2 = 5, 20, 50, 100, 250$. The two dashed curves are the separation between the close, intermediate and wide regimes. The models are labelled and marked with white filled circles.

error bars. In fact, these can vary rather widely from one telescope to another and are often underestimated by photometry software. Ignoring this effect would misrepresent the relative importance of the data sets. From this step, we choose the rescaling factors shown in Table 1, obtained by setting $\chi^2/\mathrm{dof} \simeq 1$ for each data set. We then use the rescaled data to perform a new parameter space exploration.

We then apply the fitting scheme detailed in Section 2 to our data sets. In particular, we choose a spacing between the (d, q) grid points of 0.070 in $\log d$ and 0.275 in $\log q$. For the genetic algorithm fit, we use a model population of 200 individuals evolving over 40 generations, which has proven to be enough to safely locate the regions of minimum χ^2. Finite source effects are computed using the adaptive contouring method of Dominik (2007).

The final $\chi^2(d, q)$ maps that we obtain are plotted in Fig. 2 for the intermediate and central caustic configurations, and in Fig. 3 for the intermediate and secondary caustic. The red crosses show the underlying (d, q) grid, and the blue shaded contours indicate values of $\Delta\chi^2 = 5, 20, 50, 100, 250$, where the reference model is C_s, the global best-fitting model (as obtained in Section 3.5).

3.4 Excluding minima

Fig. 4 shows a zoom on the $d < 1$ region of the χ^2 map for a source crossing a secondary caustic, with an overplot of t_E isocontours (orange lines) roughly equally spaced on a logarithmic scale. With this fitting approach, we put no initial constraints on the Einstein time t_E, though it will always remain physical ($t_E > 0$). Since we are not using any Bayesian prior for this parameter, we find that very good fits to the data are obtained with values of $t_E > 300$ d, which correspond to the minimum region in the lower left-hand part
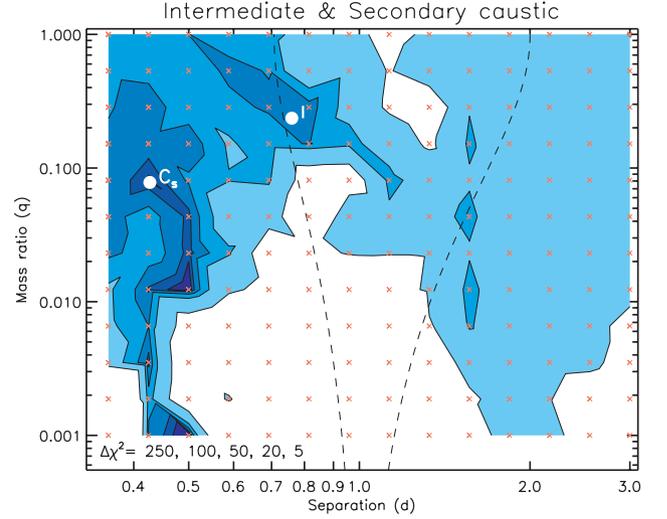
Figure 3. Same as Fig. 2, but for the intermediate and secondary caustic configuration.
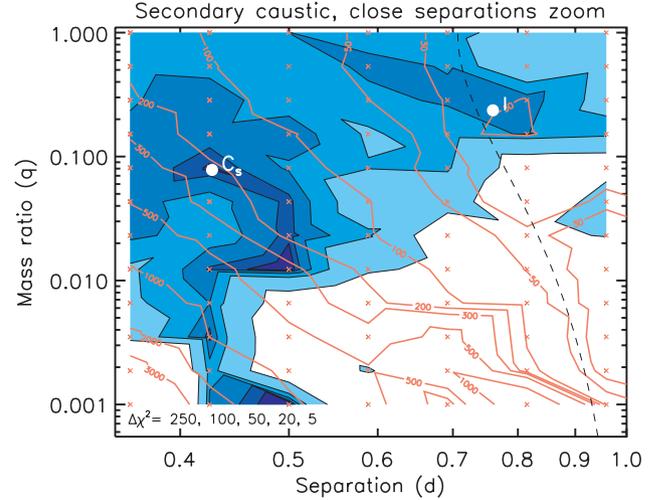
Figure 4. Map of the value of t_E in the (d, q) plane for converged models at each grid point, superimposed on the χ^2 map, zoomed in on the close regime part of parameter space. Contours lines (orange) are labelled with their corresponding value of t_E while χ^2 contour lines are plotted at $\Delta\chi^2 = 5, 20, 50, 100, 250$ and filled with gradual shades of blue. The dashed curve is the separation between the close and intermediate regimes. The models of Table 2 are labelled and marked with white filled circles.

of Fig. 3. Such long Einstein times are unlikely, and it may happen that some of the values found for t_0 correspond to a light curve that reaches its peak well in the future; these are very unlikely to be acceptable solutions. If we adopt the *posterior* t_E distribution of Dominik (2006), then $t_E > 400$ d is well in the tail of the distribution. Thus in the following, we will not consider solutions with t_E greater than 400 d. This means that we will exclude the low-q ($q \sim 0.001$) minima in the following discussion.

Although a very well-covered light curve generally enables a good characterization of the deviation caused by the caustic approach or crossing, degeneracies make finding a unique best-fitting model difficult. In particular, Griest & Safizadeh (1998) and Dominik (1999) identified a twofold degeneracy in the projected lens components separation parameter d, under the change $d \rightarrow 1/d$, when $q \ll 1$. Moreover, Kubas et al. (2005) showed that very similar

light curves could arise for a source crossing the secondary caustic of a wide binary system and for the central caustic of a close binary system. These degeneracies cause widely separated χ^2 minima in the parameter space, which must then be located by exploring the parameter space thoroughly. In addition to these degeneracies, imperfect sampling can increase the number of local χ^2 minima; short event in particular are prone to undersampling, leading to difficulties in modelling. OGLE-2007-BLG-472 is no exception, as shown in the next section.

3.5 Refining local minima

We see from Fig. 2 (intermediate and central caustic) that there are three broad local minima in the region around the white filled circles marked as C_c, I and W_c ('I', 'C' and 'W' for intermediate, close and wide models, respectively, and subscript 'c' for central caustic). In Fig. 3 (intermediate and secondary caustic), a best-fitting region can easily be located around the region marked C_s (subscript 's' for secondary caustic), besides region I.

Now allowing for the parameters d and q to vary as well, we use our MCMC algorithm to find the best solutions in each of these local minimum regions. These are identified with white filled circles in Figs 2 and 3 and correspond to the models listed in Table 2, and shown in Figs 5–8. The best model light curve is dominated by strong caustics, which all viable models must reproduce, with the low-magnification base PSPL curve barely noticeable. All models have the first anomalous OGLE points on the descending side of the caustic entry except for the worst model, model W_c, which

has this OGLE point on the ascending part of the caustic entry. Statistically, the former case is more likely to be observed since the ascending part of the caustic entry happens much more rapidly than the descending side.

Our best model, C_s, has $\chi^2 = 949$ for 975 data points, with the other competitive models at $\Delta\chi^2 = 13.2$ (model C_c), 23.5 (model I) and 39.6 (model W_c).

3.6 Parameter correlations

Fig. 4 shows that the models with a source crossing a secondary caustic have increasingly large values of t_E as they go towards lower values of the mass ratio. This is expected since the time Δt between t_{entry} and t_{exit} is fixed by the data. As the size of caustics scales with $q^{1/2}$, and $t_E \sim \Delta t/q^{1/2}$, the source must therefore cross the Einstein ring over a longer time-scale for Δt to be conserved. In addition to this, blending decreases for decreasing values of q, and therefore decreases with increasing t_E, contrary to what might be expected. Indeed, one would expect the blending factor $g = F_B/F_S$ (where F_B and F_S are the blend and source flux, respectively) to increase with increasing t_E in order to mask long time-scales and reproduce the observed time-scale. However, in this region of parameter space, the caustics are weak, which means that too much blending would not allow models to reproduce the observed rise in the source magnitude at the caustic entry and caustic exit. For a region of parameter space to contain satisfactory models, there must be a fine balance between blending, time-scale and mass ratio.

For models where the source crosses a central caustic, the impact parameter u_0 must decrease with decreasing mass ratio, since the

Table 2. Best-fitting binary-lens model parameters. The blending factor $g(I) = F_B(I)/F_S(I)$ is given for the OGLE data (I band). The error bars were rescaled for each telescope by the factor given in Table 1, which lead to the rescaled χ^2 indicated here. Physical parameters are also given for each model, for the case of a lens in the disc, and a lens in the bulge. These were calculated using the procedure detailed in Section 3.7.2.

| Parameter	Model C_s	Model C_c	Model I	Model W_c	Units
χ^2 (rescaled σ)	949.00	963.16	972.48	988.55	–
$\Delta\chi^2$	–	13.2	23.5	39.8	–
χ^2_{UTas}	23.79	24.83	26.41	28.86	–
χ^2_{Danish}	79.77	79.60	80.75	88.93	–
χ^2_{OGLE}	845.50	858.77	865.24	870.55	–
t_0	4587.18 ± 0.80	4332.27 ± 0.29	4332.10 ± 0.27	4334.99 ± 0.28	MHJD
t_E	213.82 ± 1.04	52.00 ± 3.63	38.32 ± 2.60	53.46 ± 0.81	d
α	2.810 ± 0.006	3.227 ± 0.030	3.305 ± 0.037	4.570 ± 0.018	rad
u_0	-1.573 ± 0.013	0.091 ± 0.005	0.164 ± 0.019	0.277 ± 0.010	–
$\rho_*/10^{-3}$	0.34 ± 0.01	0.98 ± 0.19	1.55 ± 0.16	1.33 ± 0.05	–
d	0.427 ± 0.002	0.673 ± 0.011	0.760 ± 0.015	2.158 ± 0.0169	–
q	0.078 ± 0.001	0.177 ± 0.017	0.236 ± 0.024	0.288 ± 0.0096	–
$g(I) = F_B(I)/F_S(I)$	7.15 ± 0.013	68.11 ± 0.013	40.13 ± 0.09	56.98 ± 0.019	–
I_s	17.89 ± 0.01	20.21 ± 0.01	19.65 ± 0.09	20.02 ± 0.01	–
I_b	15.75 ± 0.01	15.63 ± 0.01	15.64 ± 0.09	15.63 ± 0.01	–
$(V - I)_s$	1.80 ± 0.10	1.93 ± 0.11	1.91 ± 0.11	1.92 ± 0.12	–
θ_*	1.18 ± 0.24	0.46 ± 0.09	0.59 ± 0.12	0.50 ± 0.10	µas
Lens in the disc					
M_1	$1.50^{+1.85}_{-0.58}$	$0.42^{+0.40}_{-0.22}$	$0.34^{+0.36}_{-0.18}$	$0.34^{+0.37}_{-0.18}$	$M_\odot$
M_2	$0.12^{+0.14}_{-0.05}$	$0.07^{+0.07}_{-0.04}$	$0.08^{+0.08}_{-0.04}$	$0.10^{+0.11}_{-0.05}$	$M_\odot$
D_L	$1.00^{+0.95}_{-0.36}$	$5.7^{+1.1}_{-1.5}$	$6.1^{+1.1}_{-1.5}$	$6.1^{+1.0}_{-1.5}$	kpc
v	25^{+24}_{-9}	80^{+15}_{-21}	93^{+16}_{-22}	67^{+11}_{-16}	km s^{-1}
Lens in the bulge					
M_1	41^{+14}_{-14}	$1.25^{+1.47}_{-0.59}$	$0.79^{+0.93}_{-0.35}$	$0.79^{+0.94}_{-0.36}$	$M_\odot$
M_2	$3.2^{+1.1}_{-1.1}$	$0.22^{+0.26}_{-0.10}$	$0.19^{+0.22}_{-0.08}$	$0.23^{+0.27}_{-0.10}$	$M_\odot$
D_L	$6.7^{+0.4}_{-0.7}$	$7.3^{+0.6}_{-0.8}$	$7.3^{+0.6}_{-0.8}$	$7.3^{+0.6}_{-0.8}$	kpc
v	167^{+10}_{-17}	102^{+8}_{-12}	111^{+10}_{-12}	79^{+6}_{-8}	km s^{-1}
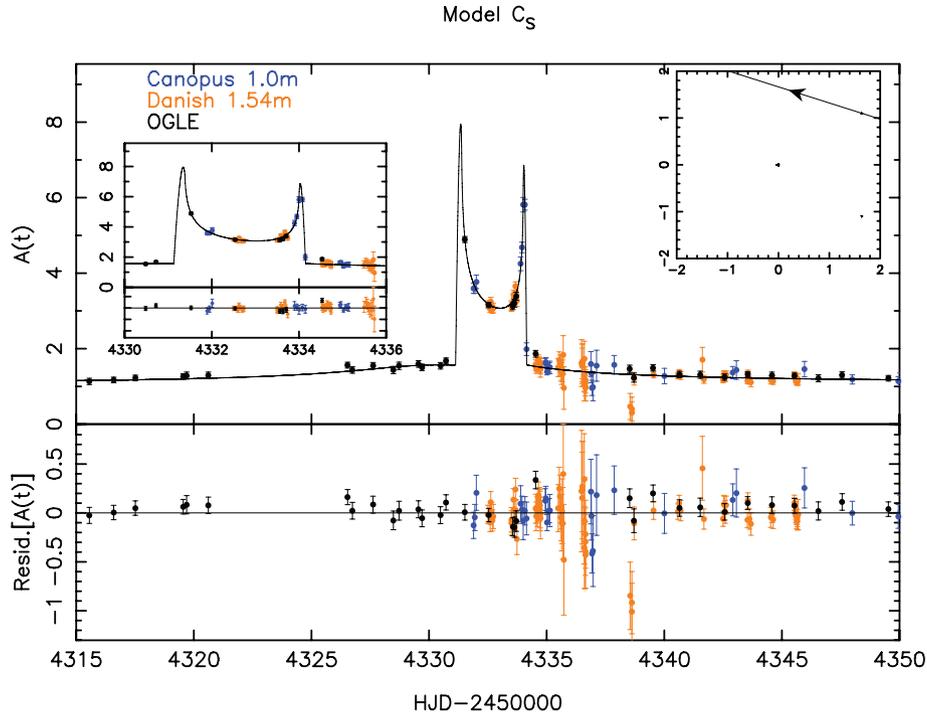
Model C$_S$

Figure 5. Best-fitting binary-lens model C_s with residuals and a zoom on the anomaly (left-hand inset). Data points are plotted with 1σ error bars. The trajectory of the source in the lens plane with the caustics is plotted as an inset in the top right-hand corner of the figure, with the primary lens component located at the coordinate system's origin.
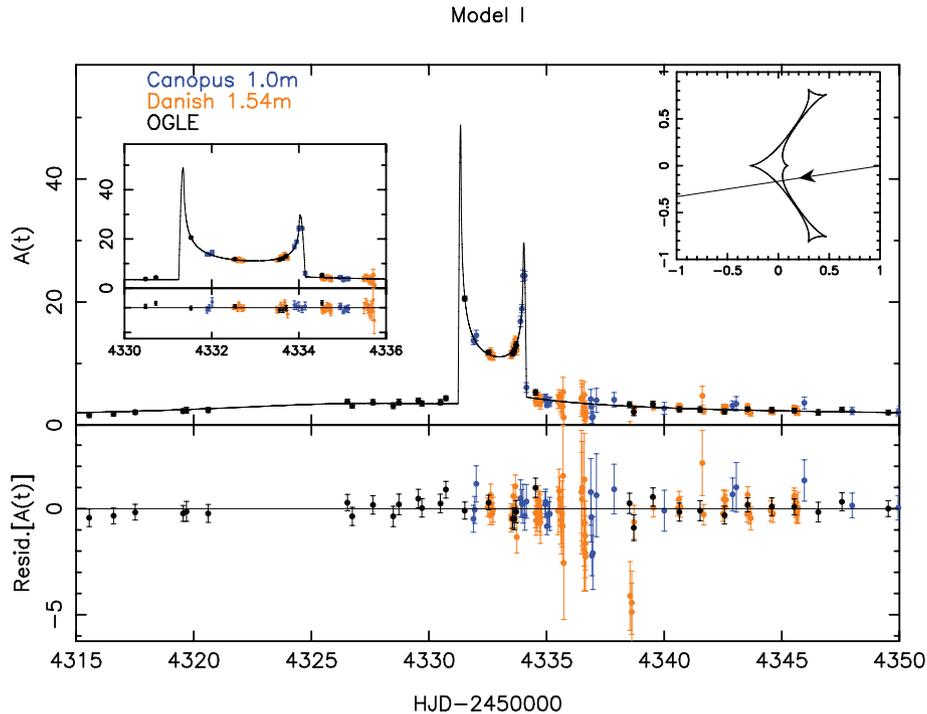
Model I

Figure 6. Same as Fig. 5, but for model *I*.

size of central caustic decreases with decreasing mass ratio, and the range of allowed u_0 decreases if the source must cross the caustic. This means that for smaller mass ratios, blending will have to increase in order to mask the correspondingly higher PSPL magnification of the source that results from the smaller impact parameter.

3.7 Physical properties of the models

3.7.1 Source characteristics

A colour–magnitude diagram (CMD) of the field (Fig. 9) was produced extracting 1497 stars from *I* and *V* images at $t = 4340.08$ (*I*)
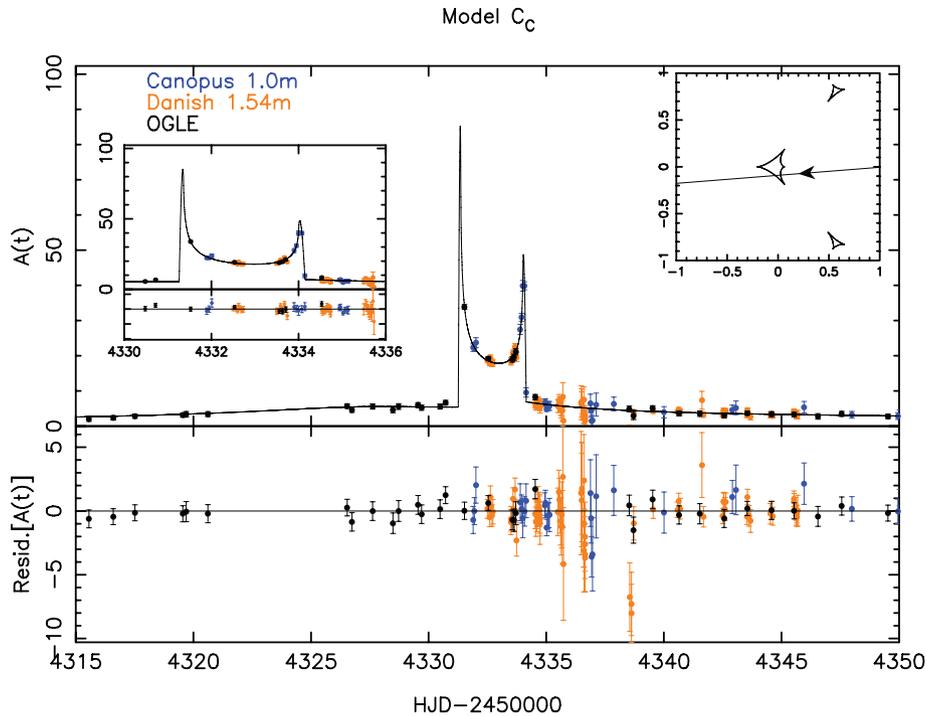
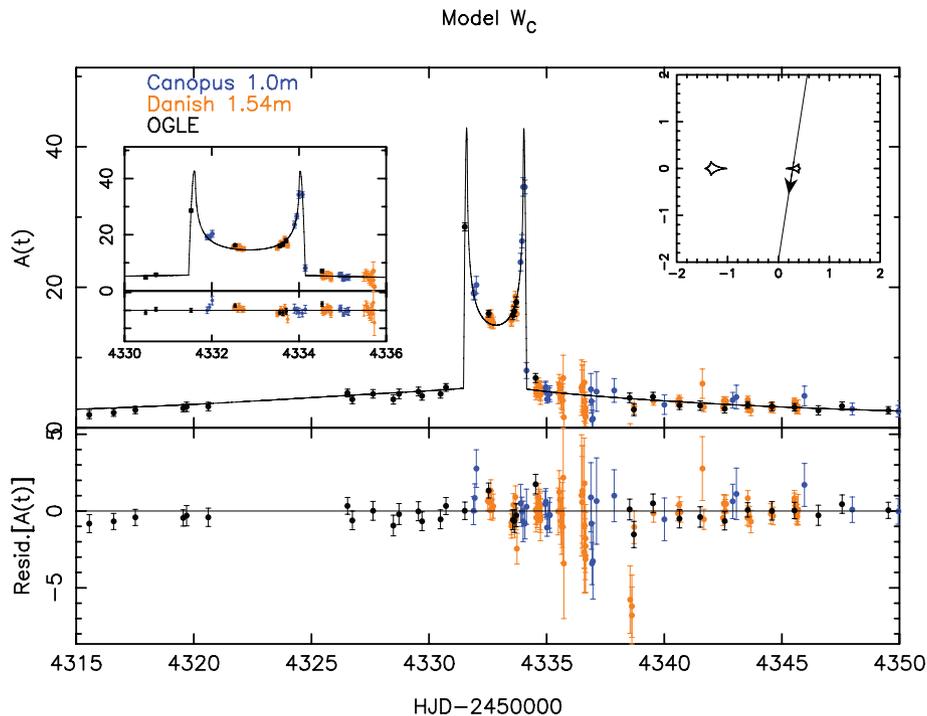**Figure 7.** Same as Fig. 5, but for model C_c.

Figure 8. Same as Fig. 5, but for model W_c.

and 4340.13 (V) taken at the Danish 1.54-m telescope. The combination of the source and the blend lies very slightly blueward of the red giant clump, at ($V - I$) = 2.43. All the models, however, are heavily blended (Table 2). The source magnitude and blending magnitude for each model can be found using the equations $I_s = I_{base} + 2.5 \log(1 + g)$ and $I_b = I_s - 2.5 \log(g)$.

Using this equation, we find source magnitudes ranging from 17.89 (model C_s) to 20.21 (model C_c) (see Table 2). Our V-band data set does not allow us to determine the source's colour, but assuming that the source is a main-sequence star, we use the calculated I magnitude of the source for each model to estimate a colour, using the results of Holtzman et al. (1998). This then enables us to estimate
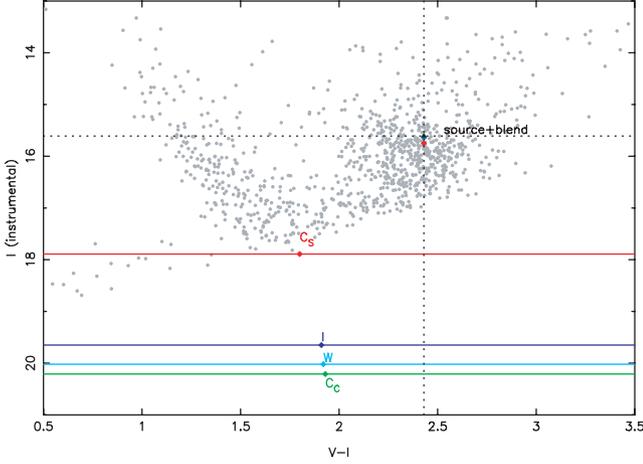
Figure 9. CMD of the field. The target OGLE-2007-BLG-472 is shown as a black triangle at $(V - I, I) = (2.43, 15.61)$. The position of the deblended source for each model is labelled and indicated by a dotted line and a coloured diamond, with the blend for each model also plotted as a diamond in the same colour.

the source's angular radius which we use in Section 3.7.2 to compute probability densities of the lensing system's properties.

We calibrate the baseline magnitude of our target (source and blend combined) using the location of the red clump as a reference. We find $I_{base} = 15.61 \pm 0.10$, which is in agreement with the OGLE value of $I_{base} = 16.00 \pm 0.50$. Comparing this to the location of the red clump, we can derive an estimate for the reddening coefficient A_I. From *Hipparcos* results, Stanek & Garnavich (1998) find an absolute magnitude for the red clump at $M_{I,RC} = -0.23 \pm 0.03$. Using a distance modulus to the Galactic centre of $\mu = 14.41 \pm 0.09$ (i.e. assuming $D_S = 7.6$ kpc; Eisenhauer et al. 2005), this translates to a dereddened magnitude for this target of $I_{base} = 14.18 \pm 0.09$. Hence using the relation $A_I = I_{base} - M_{I,RC} - \mu$, we get a value for the I-band reddening parameter of $A_I = 1.43 \pm 0.13$. Alternatively, fitting Two Micron All Sky Survey (2MASS) isochrones to our CMD, we obtain a value $A_I = 1.46 \pm 0.08$ and $E(V - I) = 1.46 \pm 0.11$. We use these values of reddening to determine dereddened magnitudes and colours for the source of each model. These, together with the surface brightness relations from Kervella & Fouqué (2008), allow us to calculate the apparent angular radius of the source θ_* for each of the models, given in Table 2.

3.7.2 Lens characteristics

Although the characteristics of any microlensing event depend on various properties of the lensing system, including the mass of the lenses, the only measurable quantity that can be directly related to physical properties of the lens is the time-scale of the event t_E. While the physical properties of the lensing system can be fully constrained when the photometry is affected by both finite source-size effects and parallax, when these are not measured, such as is the case with our analysis OGLE-2007-BLG-472, we can still use Bayesian inference to determine probability densities of physical properties of the lens, based on a chosen Galactic model. We have chosen not to include parallax in our analysis because its effect would be very small for such a low-magnification event; in addition to this, we are only seeking a first-order analysis of binary-lens events with our current method, although second-order effects such

as parallax and lens rotation will be taken into account in future work.

We use our fitted value of the source size parameter ρ_* to place constraints on the mass of the lens, which can be expressed as a function of fractional distance $x = D_L/D_S$ and the source size ρ_* as (e.g. Dominik 1998)

$$\frac{M(x)}{M_\odot} = \frac{c^2}{4G\,M_\odot} \frac{D_S\,\theta_*^2}{\rho_*^2} \frac{x}{1-x}, \tag{2}$$

where M is the mass of the lens, θ_* is the angular radius of the source, the value of which is given in Table 2, and other quantities are defined as before. The mass–distance curve showing constraints from this equation is plotted in Fig. 11.

Since we did not measure parallax for this event, we use a probabilistic approach following that of Dominik (2006) to derive probability densities for physical properties of lens components. The Galactic model used here is a piecewise mass spectrum (e.g. Chabrier 2003), two double exponentials for the disc mass density and a barred bulge tilted at an angle of $20°$ with the direction to the Galactic Centre (Dwek et al. 1995) and the distribution of effective transverse velocities used in Dominik (2006).

Using this Galactic model, we infer properties for the lensing system, separating the cases where the lens is in the Galactic disc and in the Galactic bulge. For a lens in the disc, we find a primary mass $1.50^{+1.85}_{-0.58}\,M_\odot$ and a secondary mass of $0.12^{+0.14}_{-0.05}\,M_\odot$, at a distance of $1.00^{+0.95}_{-0.36}$ kpc with a lens velocity of 25^{+24}_{-9} km s^{-1}. For a lens in the bulge, we find a primary mass $41^{+14}_{-14}\,M_\odot$ and a secondary mass of $3.2^{+1.1}_{-1.1}\,M_\odot$, at a distance of $6.7^{+0.4}_{-0.7}$ kpc with a lens velocity 167^{+10}_{-17} km s^{-1}. These are the physical lens properties for the lowest χ^2 model (model C_s). The values of these physical parameters for the other models are given in Table 2. Probability densities of these properties for all models are plotted in Fig. 10.

3.7.3 Discussion

For our lowest χ^2 model, the parameters we find imply very unusual properties of the lensing system. As discussed in Section 3.4, the fact that we find these types of models is a consequence of the fitting approach we are taking. Traditional fitting methods would struggle to find these minima, since most of them require providing a starting point in parameter space. This is an issue when solely using an MCMC algorithm to fit microlensing events: although an MCMC run may be able to make its way through parameter space to find minima reasonably far away from its starting point, it is highly unlikely that a chain will be able to reach a minimum that has significantly different parameters from the starting point. As we see from Fig. 4, there exist minima in many parts of parameter space, with values of t_E that are different by almost two orders of magnitude. These parameters are non-intuitive, since they cannot be guessed only by looking at the light curve. As a result, it is improbable that this kind of parameter will be used as starting points for 'classic' fitting algorithms.

We solve this problem for the static binary-lens case by resorting to the method described in Section 2.2. Using this approach, we manage to systematically locate minima in parameter space. However, we must then be careful with interpreting the significance of the obtained model parameters. The shape of probability densities shown in Fig. 10 for model C_s indicates that our value of t_E pushes the lens mass towards the end of the adopted mass spectrum in the Galactic model we have adopted. This results in the abrupt transitions seen in Fig. 10.
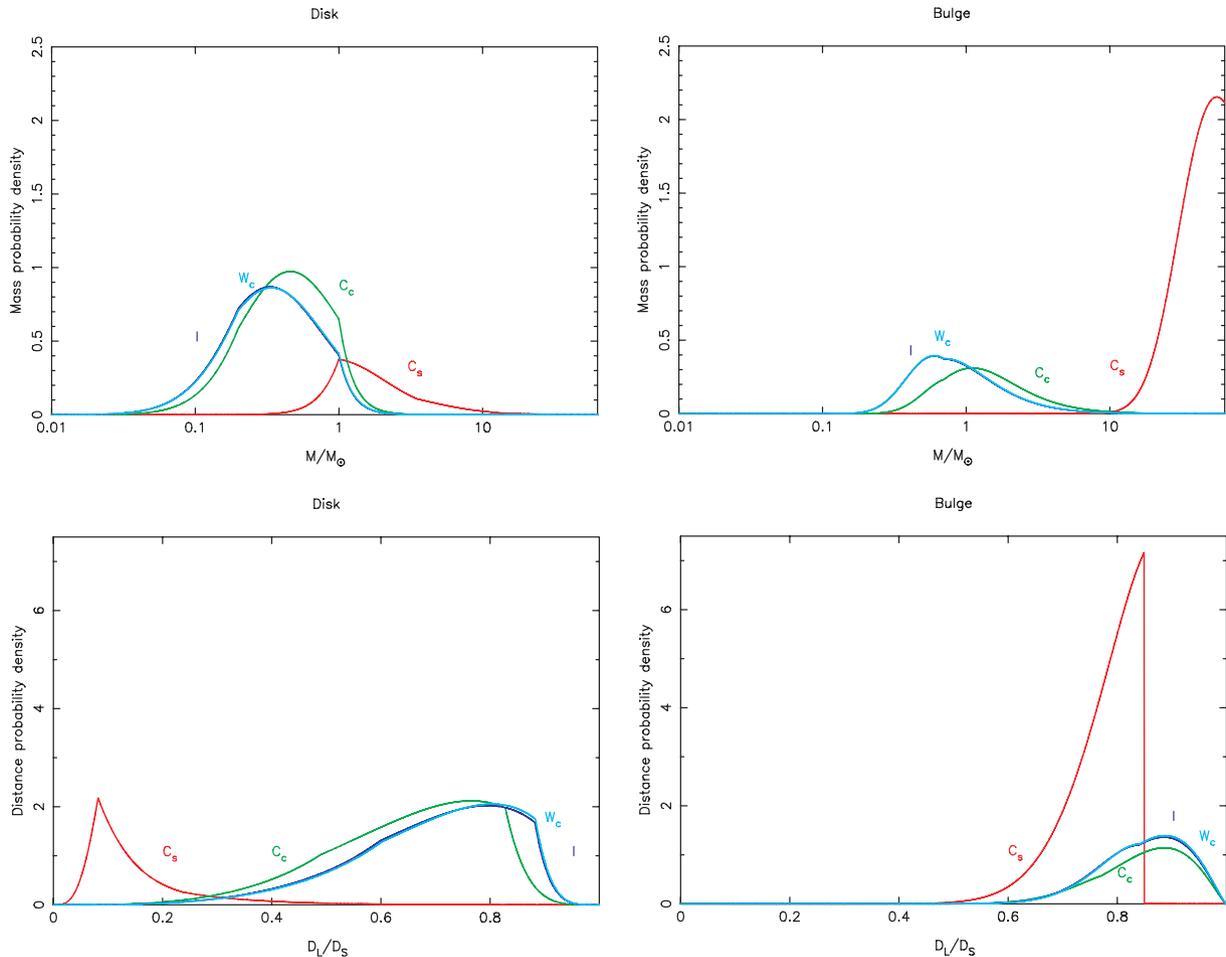
Figure 10. Probability densities for the mass of the primary lens star and the fractional distance D_L/D_S, for a lens in the disc (left-hand side) and a lens in the bulge (right-hand side). The values quoted in Table 1 are the median value and the limits of the 68.3 per cent confidence interval. On each plot, the probability densities are plotted for model C_s (red), model C_c (green), model I (dark blue) and model W_c (light blue).
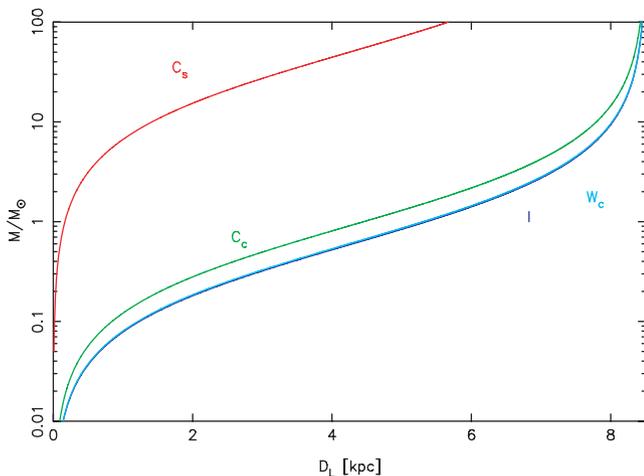

Figure 11. Mass–distance diagram showing the constraint on the lens mass from the source size, given by equation (2), for each model. The curves are labelled with the name of the model to which they correspond.

Similarly, the mass–distance curve for model C_s in Fig. 11 shows that the mass of the lens rapidly becomes very large for lenses above ~ 1 kpc. These unusual curves are caused by a value of $t_E \sim 200$ d. Models with $t_E \sim 3000$ d (corresponding to the low-q minimum vis-

ible in Figs 3 and 4) are obviously not acceptable, but how can we formally reject them? Finding these models from minima in the χ^2 surface shows the limits of using χ^2 as a strong criterion for favouring models. A solution to this would be to use prior distributions on as many of the parameters as we can. During the MCMC part of our fitting process, this would mean that we obtain posterior distributions that are different from the ones obtained without using prior distributions on the parameters, or, equivalently, assuming uniform priors for all parameters. Such priors can be obtained in various ways, such as looking at the distribution of time-scales for past microlensing events, or calculating these distributions from Galactic models (e.g. Dominik 2006) or by using luminosity functions of the Galactic bulge to find a prior for the blending factor g (e.g. Holtzman et al. 1998). Such work requires careful consideration of which priors are most appropriate to use, and is beyond the scope of this paper. Using these priors in combination with our method to find minima will lead to more robust determination of minima by taking into account our knowledge of physical parameter distributions.

4 SUMMARY AND PROSPECTS

Our analysis of OGLE-2007-BLG-472 is a good illustration of the importance and power of using parameters that are related to light-curve features. Indeed, despite incomplete coverage of the caustic

entry and high blending, a few crucial data points and an appropriate choice of non-standard parameters enable us to find several good binary-lens model fits to our data for this event by exploring the parameter space systematically. Some of the good fits that we identify have unphysical parameters, and we must then reject them. However, using this parametrization allows us to be certain that the parameter space has been thoroughly explored. We find four models with different parameters: two close binary models, one intermediate configuration and a wide binary model. The lowest χ^2 model corresponds to a G dwarf star being lensed by a binary system with component masses $M_1 = 1.50^{+1.85}_{-0.58}\,\mathrm{M}_\odot$ and $M_2 = 0.12^{+0.14}_{-0.05}\,\mathrm{M}_\odot$, which are compatible with our blending values. However, it is obvious from physical parameter distributions that using χ^2 as a sole criterion for determining the best model is insufficient, because it does not take into account our knowledge of the distributions of physical parameters.

Since the approach presented in this paper can form the basis for a systematic, wide ranging exploration of the parameter space to localize all possible models for a given data set, it is particularly relevant to current efforts to automate real-time fitting of binary-lens events. This could prove useful to provide faster feedback on events being observed, and prioritize observing schedules, especially on robotic telescopes. Expanding robotic telescope networks controlled by automated intelligent algorithms are expected to play an increasingly important role in microlensing surveys in the coming years (e.g. Tsapras et al. 2009). Fitting methods such as the one described in this paper are essential for making sure any anomalies are interpreted correctly, and that minima are located in as large a part of parameter space as possible.

REFERENCES

Bond I. A. et al., 2004, ApJ, 606, L155
Bramich D. M., 2008, MNRAS, 386, L77
Cassan A., 2008, A&A, 491, 587
Cassan A. et al., 2004, A&A, 419, L1
Chabrier G., 2003, PASP, 115, 763
Charbonneau P., 1995, ApJS, 101, 309
Dominik M., 1998, A&A, 330, 963
Dominik M., 1999, A&A, 349, 108
Dominik M., 2006, MNRAS, 367, 669
Dominik M., 2007, MNRAS, 377, 1679
Dwek E. et al., 1995, ApJ, 445, 716
Einstein A., 1936, Sci, 84, 506
Eisenhauer F. et al., 2005, ApJ, 628, 246
Erdl H., Schneider P., 1993, A&A, 268, 453
Geweke J., 1992, in Bernardo J. M., Berger J. O., David A. P., Smith A. F. M., eds, Bayesian Statistics 4: Proceedings of the Fourth Valencia International Meeting. Oxford Univ. Press, Oxford, p. 169
Ghosh H. et al., 2004, ApJ, 615, 450
Griest K., Safizadeh N., 1998, ApJ, 500, 37
Holtzman J. A., Watson A. M., Baum W. A., Grillmair C. J., Groth E. J., Light R. M., Lynds R., O'Neil E. J., Jr, 1998, AJ, 115, 1946
Jaroszynski M. et al., 2006, Acta Astron., 56, 307
Kervella P., Fouqué P., 2008, A&A, 491, 855
Kubas D. et al., 2005, A&A, 435, 941
Mao S., Paczyński B., 1991, ApJ, 374, L37
Paczyński B., 1986, ApJ, 304, 1
Stanek K. Z., Garnavich P. M., 1998, ApJ, 503, L131
Tsapras Y. et al., 2009, Astronomische Nachrichten, 330, 4
Udalski A., 2003, Acta Astron., 53, 291

This paper has been typeset from a TeX/LaTeX file prepared by the author.